Supporting Information

Santaniello et al. 10.1073/pnas.1406549111

SI Note 1: Connectivity of the Network Model

Each neuron in the network model of the cortico-BG-thalamo-cortical loop (Fig. S1) received synaptic currents (AMPA-mediated glutamatergic or $GABA_a$-mediated GABAergic) from multiple neurons. Denoted with n the generic target neuron and with I_n^{pop} the net synaptic current received by neuron n from the neuronal population *pop* (i.e., one among the populations of FSIs, MSNs, PANs, PPIs, PYNs, RENs, and TCNs), we have

$$I_n^{pop} = \frac{\bar{g}_n^{type}}{N_n^{pop}} \left(\sum_{i=1}^{N_n^{pop}} s_i \right) (V_n - E_{type}), \qquad [S1]$$

where N_n^{pop} is the number of neurons in the population *pop* that project onto the neuron n, V_n is the membrane voltage (millivolts) of neuron n, $\bar{g}_n^{type}$ is the maximal conductance in neuron n for the specific type of synapses involved (AMPA or $GABA_a$), and E_{type} is the correspondent reversal potential. The gating variable s_i, $i = 1, 2, \ldots, N_n^{pop}$ describes the presynaptic release from the projecting neuron i in the population *pop* onto the neuron n, and it evolves according to the first-order differential equation (1)

$$\frac{ds_i}{dt} = \alpha \left(1 + \tanh\left(\frac{V_i}{4} \right) \right) (1 - s_i) - \frac{s_i}{\tau}, \qquad [S2]$$

where V_i is the membrane voltage (millivolts) of the neuron i, and α and τ are parameters to be assigned. For each neuron, $E_{AMPA} = 0$ mV and $E_{GABAa} = -80$ mV, and parameters α and τ were chosen for each type of neurons to match the synaptic dynamics reported in experimental studies (Table S1). In order to increase the variability of the firing patterns at rest within each population, the values $\bar{g}_n^{AMPA}$ and $\bar{g}_n^{GABAa}$ varied with the neuron n and were extracted from a Gaussian distribution with fixed mean (Table S1) and SD equal to 10% of the mean. The connectivity among the neuron models (i.e., network topology) was defined to reflect the neuronal anatomy of the cortico-BG-thalamo-cortical loop in NHPs (2–13):

Cortico-Thalamic Subsystem. The topology of this subsystem was modified from ref. 14 to reflect the dense axonal arborization and reciprocal connections between the M1 cortex and the ventrolateral thalamus (7, 11). Each PYN received AMPA-mediated synapses from 10 PYNs (nearest neighbors) and 10 TCNs (randomly chosen) and GABAergic synapses from all of the FSIs. Each FSI had synapses from all of the remaining FSIs ($GABA_a$) and PYNs (AMPA), and three randomly chosen TCNs (AMPA). Each TCN had AMPA-mediated synapses from 10 random PYNs and GABAergic synapses from eight RENs (nearest neighbors). Each REN had synapses from all of the TCNs and RENs (AMPA- and $GABA_a$-mediated, respectively) and five randomly chosen PYNs (AMPA). Each TCN also received GABAergic input from five randomly chosen PANs from the GPi to reflect the arborization of the GPi in the ventrolateral thalamus (5, 10).

Striato-Pallidal Subsystem. This subsystem included the striatal matrix compartment (15) and it explicitly modeled the convergent inputs from the cortico-thalamic system onto the putamen (4, 8, 9, 13) and the segregated projections from the putamen to the GPi (2, 3, 6). Each MSN received AMPA-mediated synapses from five PYNs and five TCNs (randomly chosen) and $GABA_a$-mediated synapses from 10 MSNs (nearest neighbors) and all of the PPIs. Each PPI had AMPA-mediated synapses from three PYNs and three TCNs (randomly chosen) and gap junctions from six PPIs (nearest neighbors). Finally, each PAN in the GPi received $GABA_a$-mediated synapses from five random MSNs.

In both subsystems, the random connections were taken from a uniform distribution. Because the connections from the PPIs to the MSNs are more than three times larger than those among MSNs (16), the maximal conductance in Eq. **S1** for the synaptic currents from the PPIs to the MSNs was set three times the value for the synaptic currents from MSNs to MSNs, and the number of PPIs projecting to each MSN was chosen as in ref. 17. Finally, the gap junction between any two PPIs was modeled as a resistive element between them (18, 19).

The combined effects of the GABAergic synapses from GPe and the glutammatergic synpases from STN onto the GPi were simulated by endowing each PAN with a stochastic sequence of depolarizing current pulses (*SI Note 2*). Furthermore, each neuron in the network received a constant current (I_{bias}) to simulate the background excitation and a Gaussian noise with zero mean and SD σ to simulate subthreshold membrane voltage fluctuations (±5 mV). Values of I_{bias} and σ for each population are reported in Table S1. Note that, for the PYNs, the value of I_{bias} was varied across the population (Gaussian distribution with mean value reported in Table S1 and SD equal to 20% of the mean) to increase the neuron-to-neuron variability of the average discharge rate, as reported in refs. 20–22.

SI Note 2: Simulation of Normal and Parkinsonian Conditions

In normal NHPs, STN and GPe neurons have weakly correlated, nonoscillatory discharge patterns (23, 24) and the striatal MSNs receive stronger inhibition from PPIs than from other MSNs (25). We captured the latter by choosing the ratio of PPIs to MSNs (20:200) and the all-to-all connection scheme between PPIs and MSNs (*SI Note 1*) consistent with histological reports (15). We simulated the effects of the STN and GPe onto the GPi, instead, by applying to each PAN a sequence of depolarizing current pulses I_S. Each PAN received a different sequence and, within each sequence, pulses were extracted from a Poisson distribution (mean and minimum interpulse interval: 20 and 10 ms, respectively), with pulse amplitudes and durations ranging in the intervals [−9.0e-3, −5.0e-4] mA/cm^2 and [5, 10] ms, respectively (uniform distribution).

The transition from normal to parkinsonian (PD) conditions was captured by simulating the effects of the loss of dopamine in the putamen and the subthalamo-pallidal subsystem. First, we lowered the baseline current I_{bias} to the MSNs (Table S1) to simulate the effect of reduced activation of the D_1 receptors, which are primarily expressed on the MSNs along the direct pathway (26). Second, we decreased by 95% the input from the PPIs to the MSNs to simulate the effects of a reduced activation of the D_5 receptors (27). Third, we simulated the effect of the increased level of acetylcholine on the M_1 receptors of the MSNs (15) by varying the maximal conductance of the M-type potassium currents, that is, for each MSN we replaced the nominal value under normal conditions [i.e., 1.3 mS/cm^2 (1)] with a random value extracted from a Gaussian distribution with mean 1.3 mS/cm^2 and SD 0.35 mS/cm^2.

Note that the reduced activation of the D_1 receptors and the acetylcholine-mediated increased activation of the M_1 receptors have opposite effects on the excitability of the MSNs (28). In our simulations, the combination of a lower current I_{bias} and

a randomized value of the M-type maximal conductance aimed to reproduce the net effect of these mechanisms combined and it guaranteed that 10–30% of the MSNs in each instance of the network model reduced the average firing rate at the transition from normal to PD conditions.

Furthermore, we accounted for the exaggerated oscillatory input that is projected from the STN and GPe onto the GPi neurons under PD conditions (23, 29, 30) by replacing the sequences I_S applied to the PANs. Specifically, we defined two classes of pulsatile sequences (class-1 and class-2) with slightly different statistical proprieties and, for each PAN, we applied either a class-1 (60% of PANs) or a class-2 (40% of PANs) sequence of current pulses I_S. Class-1 sequences were Poisson processes (mean and minimum interpulse interval: 110 and 50 ms, respectively) with pulse amplitudes and durations varying in the range [−1.3e-2, −5.0e-4] mA/cm^2 and [20, 120] ms, respectively (uniform distribution). Class-2 sequences were Poisson processes (mean and minimum interpulse interval: 40 and 20 ms, respectively), with pulse amplitudes and durations uniformly varying in [−8.0e-3, −5.0e-4] mA/cm^2 and [20, 50] ms, respectively. Class-1 and class-2 sequences reproduced a prominent 4- to 8-Hz (i.e., tremor band) and 10- to 15-Hz (i.e., beta band) oscillatory input to the GPi neurons, respectively (23), and the ratio between class-1 and class-2 recipient PANs was chosen in agreement with the proportion reported in NHPs (23). Finally, in order to increase the pairwise correlation between pallidal neurons in PD conditions (23), we applied the same stochastic sequence I_S up to 10 PANs simultaneously.

SI Note 3: Simulation of the DBS Input

STN DBS depolarizes subthalamofugal axons projecting toward the GPi (31–33). We modeled the effects of these projections on the GPi by applying depolarizing current pulses to the PANs. For each DBS pulse every PAN received a current input $I_{DBS} = A\ w_D(t-\Delta_w)$ (triangular window) with duration $D = 3$ ms, delay $\Delta_w = 2$ ms since the pulse (Fig. S2), and amplitude A extracted from a Gaussian distribution with mean μ_{DBS} and SD equal to the mean (Table S1). Amplitude A varied with each DBS pulse and neuron and could be either supra- or subthreshold. D and Δ_w accounted for the temporal dynamics of the dendritic summation of the subthalamo-pallidal inputs in the GPi somas and the synaptic propagation latency altogether, and were chosen based on experimental data (34, 35) to reproduce the poststimulus lag observed in NHPs (36).

STN DBS is also able to depolarize cortical and thalamic neurons, presumably via antidromic mechanisms (37–39), and striatal neurons, either via orthodromic activation of the subthalamo-striatal projections (4, 40) or via antidromic activation of the striatonigral projections (6, 41). We simulated the effects of STN DBS on the thalamus, cortex, and putamen by applying depolarizing current pulses to the TCNs, PYNs, and MSNs, respectively. Current pulses were modeled as for the pallidal neurons but with shorter duration (2 ms) and delay (1 ms) to match experimental data in refs. 39, 41, 42, and 43. In particular, the delay was chosen based on experimental data (44, 45) and the duration was chosen to account for potential slow-down and gating effects occurring in the soma (44, 46). Finally, the pulse amplitude varied across the pulses and neurons and it was extracted from a Gaussian distribution with mean μ_{DBS} (Table S1) and SD equal to the mean.

Regular (i.e., constant interpulse intervals) STN DBS at 20, 50, 80, 100, 130, 160, and 180 Hz was simulated in PD conditions. Two additional scenarios were simulated in case of 130-Hz STN DBS: (*i*) ineffective regular stimulation (i.e., the mean μ_{DBS} of the distributions used to generate the amplitudes A was set to 2% of the value in Table S1 for every neural population) and (*ii*) stochastic stimulation, that is, the onsets of the DBS pulses were randomly distributed according to a Gamma function with average rate 130 Hz and 60% variability, as proposed in ref. 47.

SI Note 4: Data Analysis

Rate and Burst Analysis. For each neuron under a given combination of disease condition (i.e., normal or PD) and DBS settings we computed the mean firing rate both before and during DBS as the average discharge frequency over nonoverlapping 1,000-ms-long windows. For each population the average was then computed across the available neurons (see refs. 43 and 48).

For each neuron under a given combination of disease condition and DBS settings we defined a "burst" as a group of three or more consecutive spikes, and we detected the bursts by using the modified surprise method (49). First, we identified the putative bursts as sequences of consecutive spikes whose ISIs were less than two times the mean ISI of the series. Then we refined the putative bursts by calculating the surprise index (SI) (50) for every combination of contiguous spikes and taking the combinations with the highest SI. Finally, we rejected those refined bursts that did not include at least three consecutive spikes or that had SI <3. The mean burst rate was computed as the average number of nonrejected bursts per second over nonoverlapping 3,000-ms-long windows.

Classification of Discharge Patterns. The discharge patterns of the TCNs and PYNs under normal conditions, PD conditions with no DBS applied, and PD conditions with 130-Hz DBS were classified as "regular," "random" (i.e., irregular), or "bursty" by using the criteria in ref. 21. Briefly, for every combination of disease condition and DBS settings the spike train of each neuron was divided into consecutive, nonoverlapping intervals of length Δt (Δt is the mean ISI for the train) and the number of spikes fired in each interval (i.e., spike count) was counted. Then, we computed the fraction of intervals with spike count = 0, 1, 2, 3, etc., and we constructed the correspondent histogram. Finally, we alternatively fit the histogram with a Gaussian distribution (mean = 1, SD = 0.5) and two Poisson distributions [one having mean = 1, the other one having either mean = 0.9 (cortex) or mean = 0.8 (thalamus)]. The spike train was classified as regular, random, or bursty if the best fit (in the least square sense) was given by the Gaussian distribution, Poisson distribution with mean = 1, or the other Poisson distribution, respectively.

Poststimulus Time Histograms. For each neural population and DBS settings, we computed the PSTH by counting the neuronal discharges into consecutive nonoverlapping bins (bin size = 0.1 ms) in the interstimulus intervals following each DBS pulse and normalizing to the prestimulation baseline activity (z-score). A significant ($P < 0.01$) poststimulus increase (decrease) in neuronal discharge was indicated by the PSTH at any lag from the DBS pulse when the correspondent z-score was >2.58 (< −2.58). See ref. 48 for further details.

For each DBS setting we computed the bi-PSTH for the MSNs. First, for each simulated MSN we computed the sample histogram (bin size: 0.1 ms) of the pairs (x,y), with x and y being the latencies (in milliseconds) of the first poststimulus spike within the interpulse interval for two consecutive DBS pulses. Then, we summed the histograms across the available neurons and we normalized to the prestimulation baseline activity (z-score). A significant ($P < 0.01$) poststimulus increase (decrease) in neuronal discharge activity over two consecutive DBS pulses was indicated by the bi-PSTH at any pair of lags (x,y) when the correspondent z-score was >2.58 (< −2.58).

Cross-Correlation Analysis. For each combination of neural population, disease condition, and DBS settings we computed the average pairwise cross-correlation. Briefly, we computed the cross-correlation (maximum lag: 1,000 ms) between any pair of

neurons in the neural population and we used the maximal value of the cross-correlation sequence as estimation of the cross-correlation coefficient. Then, we estimated the sample distribution of these coefficients across the available pairs of neurons in the neural population and we computed the mean and SD.

Spectral Analysis. Power spectra of individual spike trains were computed as in ref. 51. For each combination of neuron, disease condition, and DBS settings the simulated spike trains were sampled at 1,000 Hz, filtered (PYNs, TCNs, and MSNs: ninth order low-pass Butterworth filter with 1-dB cutoff at 1 Hz; PANs: ninth order band-pass Butterworth filter with 1-dB cutoffs at 5 and 20 Hz), and tampered (Hanning window). Then, the power spectrum was computed via Welch's method as the average periodogram across consecutive windows (2,000 ms per window, 500-ms overlap), thus resulting in 0.5-Hz resolution. For each population, the average spectrum across the neurons was computed and normalized to the mean power in the band [5, 40] Hz.

For the TCNs, the MSE between the population-averaged power spectrum under normal conditions ($P_{ref}(\cdot)$) and under PD conditions with DBS [$P_{DBS_x}(\cdot)$, where x is the DBS frequency, that is, $x =$ 0, 20, 50, 80, 100, 130, 160, or 180 Hz], was computed as:

$$MSE_x = \sum_{3\le f\le 100} \frac{\left(P_{DBS_x}(f) - P_{ref}(f)\right)^2}{N}, \qquad \text{[S3]}$$

where N is the number of frequency values f in the band [3, 100] Hz at which the power spectra were estimated ($N =$ 195 because of 0.5-Hz resolution). Note that the MSE was used to measure the overall distance between the power spectra of the TCNs under different conditions, whereas the interval [3, 100] Hz was chosen because the oscillatory activity of the TCNs in several bands within this interval (e.g., tremor, beta, and gamma band) is either associated with the execution of voluntary movements or affected by movement disorders (e.g., see refs. 39 and 52–57).

Relay Performance Analysis. The fidelity of the TCNs in relaying cortical inputs was defined as in refs. 58 and 59. First, we noted that each TCN receives input from 10 different PYNs simultaneously (*SI Note 1*). Second, we noted that each TCN needs the concurrent depolarization of at least 3 out of 10 presynaptic PYNs to receive a suprathreshold depolarizing synaptic current. Hence, for each TCN in a given combination of disease condition and DBS settings we computed the total number of spikes fired in consecutive, nonoverlapping time bins (1 ms per bin) by the PYNs projecting onto that TCN, and we determined the time bins wherein three or more spikes were fired concurrently. Then, we used the concurrent presence of at least three presynaptic spikes as the minimal piece of cortical information to be relayed and we assessed whether the TCN relayed it. To the purpose, we determined whether the TCN produced a "correct response" (*CR*) to each piece of information, with the *CR* occurring if the TCN spiked at least once within $\Delta r = 30$ ms since the delivery of the piece. Finally, we measured the relay fidelity of the TCN by computing the fidelity index (*FI*) (59):

$$FI = \frac{\#CR}{N_{bins}}, \qquad \text{[S4]}$$

where N_{bins} is the number of time bins with three or more concurrent cortico-thalamic inputs to that TCN. For each TCN, disease condition, and DBS settings, we computed the average *FI* value over consecutive, nonoverlapping $W =$ 3,000-ms-long windows. Variation of ±10% in the size of Δr and W did not significantly affect the results of our analysis.

We used the average *FI* (mean and SD) across all of the TCNs under normal conditions (no DBS applied) as a reference (FI_{ref}) and we compared the values of *FI* under PD conditions (either with or without DBS) to this reference. In particular, for any DBS settings under PD conditions, we computed the loss in fidelity as

$$loss = 100 \times \left| \frac{FI - \mu_{ref}}{\sigma_{ref}} \right|, \qquad \text{[S5]}$$

with μ_{ref} and σ_{ref} being the mean and SD of the reference error FI_{ref}.

SI Note 5: Population-Average Discharge Patterns and Cross-Correlation

Fig. S3 reports the population-average firing rates for the PYNs, TCNs, MSNs, and PANs in the model under different disease conditions and DBS settings (regular stimulation applied).

Fig. S4 reports the percentage of PYNs, TCNs, MSNs, and PANs under PD conditions that had significant poststimulus modulation of the discharge activity under regular DBS. In particular, we first computed the PSTH normalized to the prestimulation activity (z-score) for each neuron under 20-, 50-, and 130-Hz DBS. Then, for each DBS frequency, we analyzed the PSTHs and, for each bin (bin size: 0.1 ms), we counted how many PYNs, TCNs, MSNs, and PANs had a z-score higher than 1.96 in that bin. Finally, we plotted the percentage of neurons in each neural population having a z-score higher than 1.96 in each bin. Note that a z-score higher than 1.96 means that the likelihood of having a spike in that bin is significantly higher during stimulation than before stimulation, with a P value $P < 0.05$.

Fig. S5 assesses the direct effects of STN DBS on the poststimulus activity of PYNs and TCNs. In particular, we computed the PSTH for PYNs and TCNs under 130-Hz STN DBS for the following simulated scenarios:

i) The network model was simulated under PD conditions and the direct effects of 130-Hz DBS were applied to the PANs, PYNs, TCNs, and MSNs.
ii) The network model was simulated under PD conditions and the direct effects of 130-Hz DBS were applied to the PANs, TCNs, and MSNs, but not to the PYNs.
iii) The network model was simulated under PD conditions and the direct effects of 130-Hz DBS were applied to the PANs, PYNs, and MSNs, but not to the TCNs.

Each scenario was simulated three times (hence the number of PYNs and TCNs in Fig. S5 is $N = 600$). Fig. S5 indicates that the poststimulus activation of the neurons is primarily due to the direct effects of DBS.

For each combination of disease condition and DBS settings we estimated the cross-correlation coefficient for every pair of PANs, PYNs, TCNs, or MSNs. It resulted that, for the PYNs, the cross-correlation decreased when transitioning from normal to PD conditions and then it increased when DBS was applied (normal: 1.56e-4 ± 0.94e-4; PD with no DBS: 1.41e-4 ± 0.86e-4; PD with 130-Hz STN DBS: 3.03e-4 ± 1.26e-4; mean ± SD). The pairwise cross-correlation of the TCNs increased under PD conditions and was restored to the value for the normal state when high-frequency DBS was applied (normal: 4.15e-4 ± 3.53e-4; PD with no DBS: 5.03e-4 ± 4.19e-4; PD with 130-Hz STN DBS: 4.19e-4 ± 4.30e-4; mean ± SD). The trend for PANs and MSNs was as follows (mean ± SD):

- PANs: 4.64e-3 ± 0.19e-3 (normal); 7.26e-3 ± 0.93e-3 (PD with no DBS); 1.37e-2 ± 0.08e-2 (PD with 130-Hz STN DBS).
- MSNs: 6.0e-5 ± 2.8e-5 (normal); 1.52e-4 ± 0.95e-4 (PD with no DBS); 2.46e-4 ± 1.41e-4 (PD with 130-Hz STN DBS).

We simulated the model under PD conditions and regular 130-Hz STN DBS while blocking the synaptic currents from the MSNs to

the PANs and replacing these currents with a surrogate input (open-loop simulation; see main text for details). Then, for every PAN, we computed the firing rates in nonoverlapping 1,000-ms-long windows and we compared with the correspondent values obtained without the synaptic block from the MSNs to the PANs. Results are reported in Fig. S6.

SI Note 6: Snapshots of the Simulated Model Network

Fig. S7 reports the raster plots over a 500-ms window of the cortical neurons (PYNs and FSIs), thalamic neurons (TCNs and RENs), striatal neurons (MSNs and PPIs), and pallidal neurons (PANs) in our model network under normal conditions and PD conditions (no DBS applied), and under PD conditions with 130-Hz STN DBS (60, 61).

1. McCarthy MM, et al. (2011) Striatal origin of the pathologic beta oscillations in Parkinson's disease. *Proc Natl Acad Sci USA* 108(28):11620–11625.
2. Smith Y, Parent A (1986) Differential connections of caudate nucleus and putamen in the squirrel monkey (Saimiri sciureus). *Neuroscience* 18(2):347–371.
3. Giménez-Amaya JM, Graybiel AM (1990) Compartmental origins of the striatopallidal projection in the primate. *Neuroscience* 34(1):111–126.
4. Nakano K, et al. (1990) Topographical projections from the thalamus, subthalamic nucleus and pedunculopontine tegmental nucleus to the striatum in the Japanese monkey, Macaca fuscata. *Brain Res* 537(1-2):54–68.
5. Hazrati LN, Parent A (1991) Contralateral pallidothalamic and pallidotegmental projections in primates: An anterograde and retrograde labeling study. *Brain Res* 567(2):212–223.
6. Hedreen JC, DeLong MR (1991) Organization of striatopallidal, striatonigral, and nigrostriatal projections in the macaque. *J Comp Neurol* 304(4):569–595.
7. Rouiller EM, et al. (1998) Dual morphology and topography of the corticothalamic terminals originating from the primary, supplementary motor, and dorsal premotor cortical areas in macaque monkeys. *J Comp Neurol* 396(2):169–185.
8. McFarland NR, Haber SN (2000) Convergent inputs from thalamic motor nuclei and frontal cortical areas to the dorsal striatum in the primate. *J Neurosci* 20(10): 3798–3813.
9. McFarland NR, Haber SN (2001) Organization of thalamostriatal terminals from the ventral motor nuclei in the macaque. *J Comp Neurol* 429(2):321–336.
10. Parent M, Lévesque M, Parent A (2001) Two types of projection neurons in the internal pallidum of primates: Single-axon tracing and three-dimensional reconstruction. *J Comp Neurol* 439(2):162–175.
11. McFarland NR, Haber SN (2002) Thalamic relay nuclei of the basal ganglia form both reciprocal and nonreciprocal cortical connections, linking multiple frontal cortical areas. *J Neurosci* 22(18):8117–8132.
12. Shepherd GM (2004) *The Synaptic Organization of the Brain* (Oxford Univ Press, New York).
13. Parent M, Parent A (2006) Single-axon tracing study of corticostriatal projections arising from primary motor cortex in primates. *J Comp Neurol* 496(2):202–213.
14. Destexhe A, Contreras D, Steriade M (1998) Mechanisms underlying the synchronizing action of corticothalamic feedback through inhibition of thalamic relay cells. *J Neurophysiol* 79(2):999–1016.
15. Kreitzer AC (2009) Physiology and pharmacology of striatal neurons. *Annu Rev Neurosci* 32:127–147.
16. Planert H, Szydlowski SN, Hjorth JJ, Grillner S, Silberberg G (2010) Dynamics of synaptic transmission between fast-spiking interneurons and striatal projection neurons of the direct and indirect pathways. *J Neurosci* 30(9):3499–3507.
17. Koós T, Tepper JM (1999) Inhibitory control of neostriatal projection neurons by GABAergic interneurons. *Nat Neurosci* 2(5):467–472.
18. Hjorth J, Blackwell KT, Kotaleski JH (2009) Gap junctions between striatal fast-spiking interneurons regulate spiking activity and synchronization as a function of cortical activity. *J Neurosci* 29(16):5276–5286.
19. Klaus A, et al. (2011) Striatal fast-spiking interneurons: From firing patterns to postsynaptic impact. *Front Syst Neurosci* 5:57.
20. Goldberg JA, et al. (2002) Enhanced synchrony among primary motor cortex neurons in the 1-methyl-4-phenyl-1,2,3,6-tetrahydropyridine primate model of Parkinson's disease. *J Neurosci* 22(11):4639–4653.
21. Pasquereau B, Turner RS (2011) Primary motor cortex of the parkinsonian monkey: Differential effects on the spontaneous activity of pyramidal tract-type neurons. *Cereb Cortex* 21(6):1362–1378.
22. Pessiglione M, et al. (2005) Thalamic neuronal activity in dopamine-depleted primates: Evidence for a loss of functional segregation within basal ganglia circuits. *J Neurosci* 25(6):1523–1531.
23. Raz A, Vaadia E, Bergman H (2000) Firing patterns and correlations of spontaneous discharge of pallidal neurons in the normal and the tremulous 1-methyl-4-phenyl-1,2,3,6-tetrahydropyridine vervet model of parkinsonism. *J Neurosci* 20(22):8559–8571.
24. Wichmann T, Bergman H, DeLong MR (1994) The primate subthalamic nucleus. I. Functional properties in intact animals. *J Neurophysiol* 72(2):494–506.
25. Koós T, Tepper JM, Wilson CJ (2004) Comparison of IPSCs evoked by spiny and fast-spiking neurons in the neostriatum. *J Neurosci* 24(36):7916–7922.
26. Ince E, Ciliax BJ, Levey AI (1997) Differential expression of D1 and D2 dopamine and m4 muscarinic acetylcholine receptor proteins in identified striatonigral neurons. *Synapse* 27(4):357–366.
27. Centonze D, et al. (2003) Receptor subtypes involved in the presynaptic and postsynaptic actions of dopamine on striatal interneurons. *J Neurosci* 23(15):6245–6254.
28. Mallet N, Ballion B, Le Moine C, Gonon F (2006) Cortical inputs and GABA interneurons imbalance projection neurons in the striatum of parkinsonian rats. *J Neurosci* 26(14):3875–3884.
29. Bergman H, Wichmann T, Karmon B, DeLong MR (1994) The primate subthalamic nucleus. II. Neuronal activity in the MPTP model of parkinsonism. *J Neurophysiol* 72(2):507–520.
30. Wichmann T, Bergman H, DeLong MR (1994) The primate subthalamic nucleus. III. Changes in motor behavior and neuronal activity in the internal pallidum induced by subthalamic inactivation in the MPTP model of parkinsonism. *J Neurophysiol* 72(2): 521–530.
31. McIntyre CC, Grill WM (1999) Excitation of central nervous system neurons by nonuniform electric fields. *Biophys J* 76(2):878–888.
32. McIntyre CC, Grill WM, Sherman DL, Thakor NV (2004) Cellular effects of deep brain stimulation: Model-based analysis of activation and inhibition. *J Neurophysiol* 91(4):1457–1469.
33. Miocinovic S, et al. (2006) Computational analysis of subthalamic nucleus and lenticular fasciculus activation during therapeutic deep brain stimulation. *J Neurophysiol* 96(3):1569–1580.
34. Hanson JE, Smith Y, Jaeger D (2004) Sodium channels and dendritic spike initiation at excitatory synapses in globus pallidus neurons. *J Neurosci* 24(2):329–340.
35. Jaeger D, Kita H (2011) Functional connectivity and integrative properties of globus pallidus neurons. *Neuroscience* 198:44–53.
36. Saxena S, Santaniello S, Montgomery EB, Jr, Gale JT, Sarma SV (2010) Point process models show temporal dependencies of basal ganglia nuclei under deep brain stimulation. *Conf Proc IEEE Eng Med Biol Soc* 2010:4152–4155.
37. Li Q, et al. (2012) Therapeutic deep brain stimulation in parkinsonian rats directly influences motor cortex. *Neuron* 76(5):1030–1041.
38. Li S, Arbuthnott GW, Jutras MJ, Goldberg JA, Jaeger D (2007) Resonant antidromic cortical circuit activation as a consequence of high-frequency subthalamic deep-brain stimulation. *J Neurophysiol* 98(6):3525–3537.
39. Xu W, Russo GS, Hashimoto T, Zhang J, Vitek JL (2008) Subthalamic nucleus stimulation modulates thalamic neuronal activity. *J Neurosci* 28(46):11916–11924.
40. Smith Y, Hazrati LN, Parent A (1990) Efferent projections of the subthalamic nucleus in the squirrel monkey as studied by the PHA-L anterograde tracing method. *J Comp Neurol* 294(2):306–323.
41. Montgomery EB, Jr, Gale JT (2008) Mechanisms of action of deep brain stimulation (DBS). *Neurosci Biobehav Rev* 32(3):388–407.
42. Santaniello S, Gale JT, Montgomery EB, Jr, Sarma SV (2012) Reinforcement mechanisms in putamen during high frequency STN DBS: A point process study. *Conf Proc IEEE Eng Med Biol Soc* 2012:1214–1217.
43. Santaniello S, Montgomery EB, Jr, Gale JT, Sarma SV (2012) Non-stationary discharge patterns in motor cortex under subthalamic nucleus deep brain stimulation. *Front Integr Neurosci* 6:35.
44. Chomiak T, Hu B (2007) Axonal and somatic filtering of antidromically evoked cortical excitation by simulated deep brain stimulation in rat brain. *J Physiol* 579(Pt 2): 403–412.
45. Walker HC, et al. (2012) Short latency activation of cortex during clinically effective subthalamic deep brain stimulation for Parkinson's disease. *Mov Disord* 27(7):864–873.
46. Grill WM, Cantrell MB, Robertson MS (2008) Antidromic propagation of action potentials in branched axons: implications for the mechanisms of action of deep brain stimulation. *J Comput Neurosci* 24(1):81–93.
47. Dorval AD, Kuncel AM, Birdno MJ, Turner DA, Grill WM (2010) Deep brain stimulation alleviates parkinsonian bradykinesia by regularizing pallidal activity. *J Neurophysiol* 104(2):911–921.
48. Montgomery EB, Jr (2006) Effects of GPi stimulation on human thalamic neuronal activity. *Clin Neurophysiol* 117(12):2691–2702.
49. Hahn PJ, et al. (2008) Pallidal burst activity during therapeutic deep brain stimulation. *Exp Neurol* 211(1):243–251.
50. Legéndy CR, Salcman M (1985) Bursts and recurrences of bursts in the spike trains of spontaneously active striate cortex neurons. *J Neurophysiol* 53(4):926–939.
51. Moran A, Stein E, Tischler H, Bar-Gad I (2012) Decoupling neuronal oscillations during subthalamic nucleus stimulation in the parkinsonian primate. *Neurobiol Dis* 45(1): 583–590.
52. Jenkinson N, Kühn AA, Brown P (2013) Gamma oscillations in the human basal ganglia. *Exp Neurol* 245:72–76.
53. Ribary U (2005) Dynamics of thalamo-cortical network oscillations and human perception. *Prog Brain Res* 150:127–142.
54. Lenz FA, et al. (1990) Single unit analysis of the human ventral thalamic nuclear group. Activity correlated with movement. *Brain* 113(Pt 6):1795–1821.
55. Lenz FA, et al. (1994) Single unit analysis of the human ventral thalamic nuclear group. Tremor-related activity in functionally identified cells. *Brain* 117(Pt 3):531–543.
56. Lenz FA, et al. (1988) Single unit analysis of the human ventral thalamic nuclear group: Correlation of thalamic "tremor cells" with the 3-6 Hz component of parkinsonian tremor. *J Neurosci* 8(3):754–764.
57. Zirh TA, Lenz FA, Reich SG, Dougherty PM (1998) Patterns of bursting occurring in thalamic cells during parkinsonian tremor. *Neuroscience* 83(1):107–121.
58. Guo Y, Rubin JE, McIntyre CC, Vitek JL, Terman D (2008) Thalamocortical relay fidelity varies across subthalamic nucleus deep brain stimulation protocols in a data-driven computational model. *J Neurophysiol* 99(3):1477–1492.
59. Agarwal R, Sarma SV (2012) Performance limitations of relay neurons. *PLOS Comput Biol* 8(8):e1002626.
60. Destexhe A, Bal T, McCormick DA, Sejnowski TJ (1996) Ionic mechanisms underlying synchronized oscillations and propagating waves in a model of ferret thalamic slices. *J Neurophysiol* 76(3):2049–2070.
61. Chuhma N, Tanaka KF, Hen R, Rayport S (2011) Functional connectome of the striatal medium spiny neuron. *J Neurosci* 31(4):1183–1192.

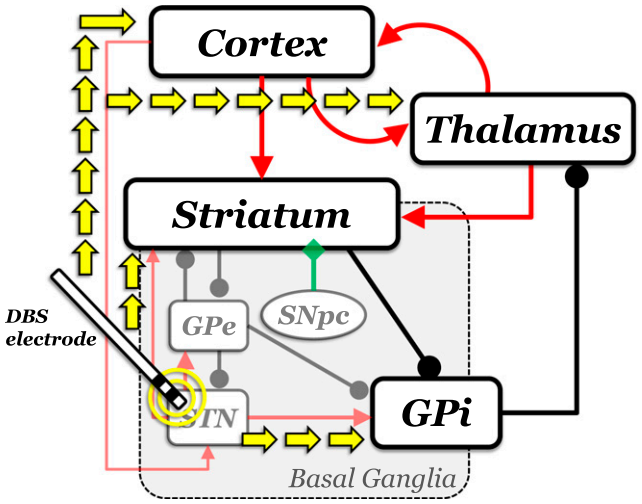

Fig. S1. Schematic of the cortico-BG-thalamo-cortical loop with the direct effects of STN DBS on cortex, striatum, GPi, and thalamus (yellow arrows). Red, black, and green arrows are glutamatergic, GABAergic, and dopaminergic projections, respectively. The structures explicitly modeled are depicted with black boxes, and the remaining structures are in gray boxes. Legend: GPe (GPi), external (internal) globus pallidus; SNpc, substantia nigra pars compacta; STN, subthalamic nucleus.

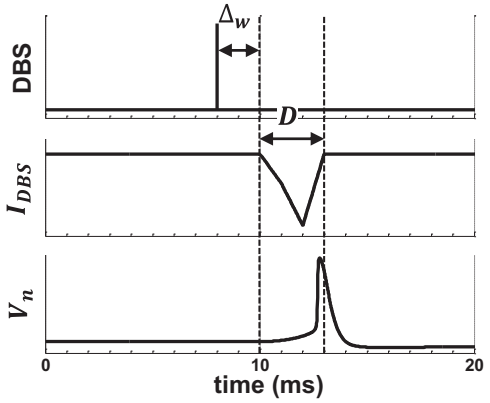

Fig. S2. Schematic of the simulation of the effects of a STN DBS pulse onto a GPi neuron. When the DBS pulse is delivered (*Top*), a delayed poststimulus current (I_{DBS}) is applied to the neuron, where the delay Δ_W and the duration D of the current mimic the propagation of the pulse from the STN to the presynaptic area of the neuron and the postsynaptic inflow, respectively. If I_{DBS} is suprathreshold, the membrane potential V_n of the neuron results in an action potential.

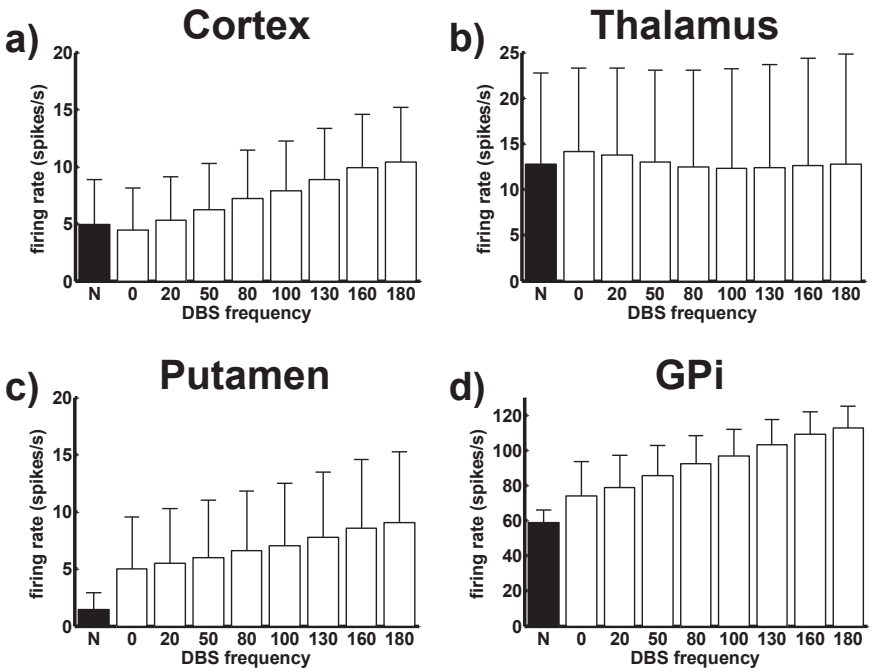

Fig. S3. Population-average firing rate (mean + SD) of PYNs (*A*), TCNs (*B*), MSNs (*C*), and PANs (*D*) in normal conditions at rest (N) and in PD conditions with regular DBS applied at several frequencies. Each population includes $N = 600$ neurons. 0-Hz DBS means no stimulation applied.

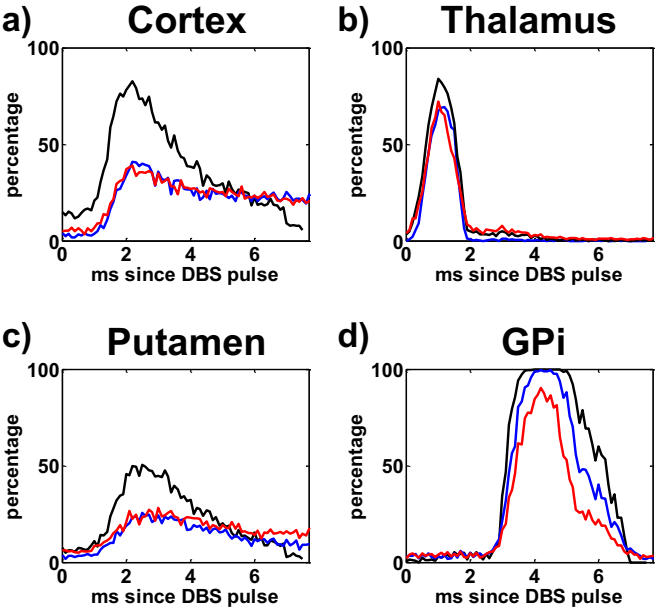

Fig. S4. Percentages of PYNs (*A*), TCNs (*B*), MSNs (*C*), and PANs (*D*) simulated under PD conditions whose PSTH has a z-score higher than 1.96 when DBS at 20 Hz (red lines), 50 Hz (blue lines), and 130 Hz (black lines) is applied. Each population includes $N = 600$ neurons.

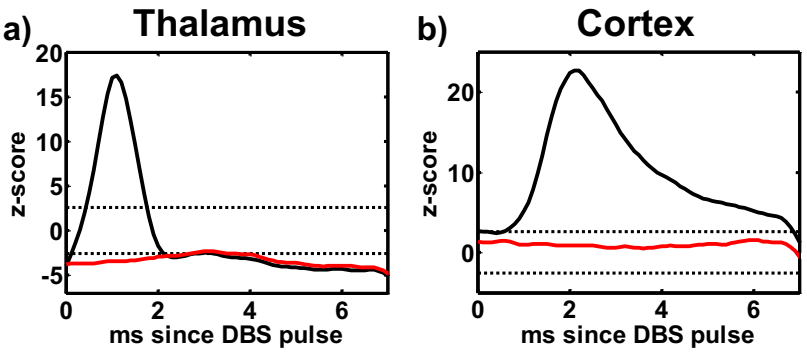

Fig. S5. PSTH (bin width: 0.2 ms) of TCNs (*A*) and PYNs (*B*) estimated under PD conditions with 130-Hz STN DBS. Black lines are computed for scenario *i* in *SI Note 5*. Red lines are computed for scenarios *iii* and *ii* in *SI Note 5*, respectively. Black dotted lines denote the 95% confidence bounds.

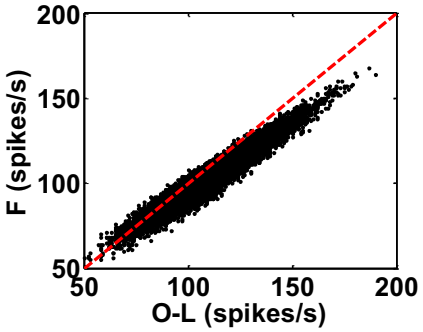

Fig. S6. Each dot reports the discharge rate of a PAN ($N = 600$ neurons) in a nonoverlapping 1,000-ms-long window for two DBS settings, i.e., F (*y* axis) and O-L (*x* axis). Settings: F, PD conditions and regular 130-Hz STN DBS applied (antidromic and orthodromic effects included); O-L, as settings F but the synaptic currents from the MSNs to the PANs are blocked and replaced by a surrogate input (open-loop simulation).

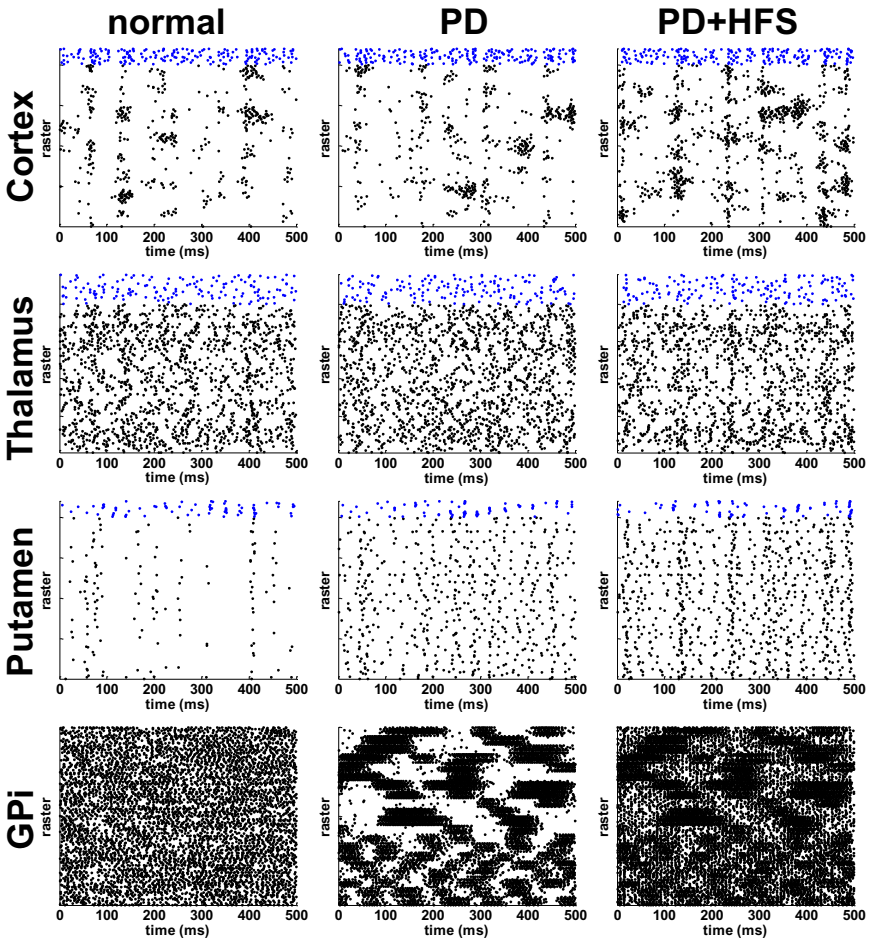

Fig. S7. Raster plot of the simulated model neurons under normal conditions (left column), PD conditions with no stimulation (center column), and PD conditions with 130-Hz STN DBS (PD+HFS, left column). From top to bottom: PYNs (black dots) and FSIs (blue dots) in the cortex; TCNs (black dots) and RENs (blue dots) in the thalamus; MSNs (black dots) and PPIs (blue dots) in the putamen; PANs in the GPi.

Table S1. Parameters in the model

Neuron type	I_{bias}, mA/cm^2	μ_{DBS}, mA/cm^2	σ Gaussian noise, mA/cm^2	$\langle \bar{g}_{type} \rangle$, S/cm^2	Synaptic gate s	Refs.
PYN	−1.88e-3	−3.5e-3	−1.0e-3	2.7e-4 (AMPA) 3.6e-4 ($GABA_a$)	To PYNs, FSIs, TCNs RENs: $\alpha = 0.55$; $\tau = 5.26$ ms To MSNs: $\alpha = 0.2$; $\tau = 16.7$ ms To PPIs: $\alpha = 0.23$; $\tau = 2.38$ ms	14 18 16, 19
FSI	−2.0e-3	NA	−1.0e-3	2.9e-4 (AMPA) 1.0e-4 ($GABA_a$)	To PYNs, FSIs: $\alpha = 2.5$; $\tau = 5.56$ ms	14
TCN	−3.0e-3	−4.0e-3	−7.0e-4	3.7e-4 (AMPA) 1.6e-4 ($GABA_a$)	To PYNs, FSIs, RENs: $\alpha = 0.55$; $\tau = 5.26$ ms To MSNs: $\alpha = 0.2$; $\tau = 11.1$ ms To PPIs: $\alpha = 0.23$; $\tau = 2.38$ ms	14 18 16, 19
REN	−1.0e-3	NA	−7.0e-4	1.0e-4 (AMPA) 8.0e-4 ($GABA_a$)	To RENs, TCNs: $\alpha = 10$; $\tau = 6.17$ ms	60
MSN	−5.0e-4* −3.5e-4**	−1.7e-3	−7.0e-4	1.3e-4 (AMPA) 3.5e-4 ($GABA_a$)† 1.0e-3 ($GABA_a$)§	To MSNs, PANs: $\alpha = 2.0$; $\tau = 13.0$ ms	1
PPI	−3.0e-3	NA	−1.0e-3	1.0e-4 (AMPA) 2.0e-4 ($GABA_a$)	To MSNs: $\alpha = 2.0$; $\tau = 13.0$ ms	61
PAN	NA	−4.3e-3	−1.0e-3	3.4e-4 ($GABA_a$)	To TCNs: $\alpha = 10$; $\tau = 6.17$ ms	60

$\langle \bar{g}_{type} \rangle$, mean value of the maximal conductance ("type" is either AMPA or $GABA_a$) in the neurons of the type specified in the first column; s, gating variable in Eq. **S2** from the neurons of the type specified in the first column. For each type of target neuron, α and τ are reported along with the correspondent reference (last column). †Synapses from MSNs; §synapses from PPIs; *normal state; **PD state; NA, not applied. Note that I_{bias} is the average value in case of PYNs.